ACSNANO

www.acsnano.org

ARTICLE

Photothermomechanical Nanopump: A Flow-Through Plasmonic Sensor at the Fiber Tip

Nabarun Polley,* Samim Sardar, Peter Werner, Ingo Gersonde, Yuya Kanehira, Ilko Bald, Daniel Repp, Thomas Pertsch, and Claudia Pacholski*

Cite This: *ACS Nano* 2023, 17, 1403−1413

Read Online

ACCESS | Metrics & More | Article Recommendations | Supporting Information

ABSTRACT: **Optical fibers equipped with plasmonic flow sensors at their tips are fabricated and investigated as photothermomechanical nanopumps for the active transport of target analytes to the sensor surface. The nanopumps are prepared using a bottom-up strategy: i.e., by sequentially stacking a monolayer of a thermoresponsive polymer and a plasmonic nanohole array on an optical fiber tip. The temperature-dependent collapse and swelling of the polymer is used to create a flow-through pumping mechanism. The heat required for pumping is generated by exploiting the photothermal effect in the plasmonic nanohole array upon irradiation with laser light (405 nm). Simultaneous detection of analytes by the plasmonic sensor is achieved by monitoring changes in its optical response at longer wavelengths (~500−800 nm). Active mass transport by pumping through the holes of the plasmonic nanohole array is visualized by particle imaging velocimetry. Finally, the performance of the photothermomechanical nanopumps is investigated for two types of analytes, namely nanoscale objects (gold nanoparticles) and molecules (11-mercaptoundecanoic acid). In the presence of the pumping mechanism, a 4-fold increase in sensitivity was observed compared to the purely photothermal effect, demonstrating the potential of the presented photothermomechanical nanopumps for sensing applications.**

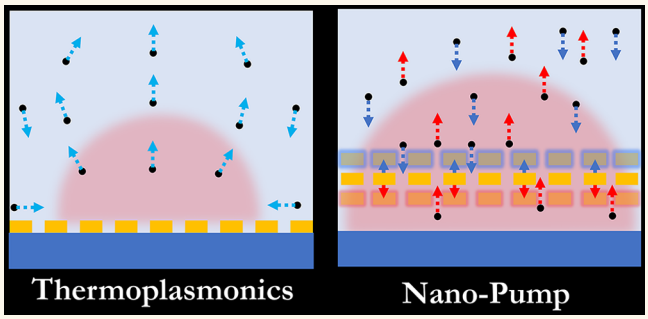

KEYWORDS: *photothermal effect, thermoresponsive polymer, flow-through sensing, self-assembly, nanohole array, surface plasmon resonance, optical fiber sensor*

INTRODUCTION

Small and portable sensors are key to many application areas, such as environmental monitoring,[1] food monitoring,[2] industrial monitoring,[3] and biomedical/clinical studies.[4] In this context, sensors using surface plasmon resonance (SPR) have emerged as label-free technologies that monitor a change in refractive index due to the trapping of molecules on the plasmonic surface, allowing the detection of a wide range of molecules.[5,6] Nanostructured plasmonic sensors may offer several advantages, as they can confine and enhance subwavelength electromagnetic fields compared to established techniques based on surface plasmon resonance with a flat metal surface. Nanochip arrays have been increasingly investigated as optical sensors since Ebbesen et al. reported extraordinary optical transmission through nanohole arrays (NHAs) in the subwavelength range.[7] The tunability and flexibility of NHAs has enabled the development of wearable and innovative medical devices for point-of-care (POC) applications.[8] More recently, the integration of NHAs into optical fibers has resulted in a portable and cost-effective optical platform where light transmission and signal acquisition are simpler and more efficient.[9−11]

However, there is still room for improvement in terms of detection time and sensitivity. One promising strategy for optimizing the performance of NHA sensors is the targeted delivery and concentration of analytes to the interior of the nanoholes, the site of the NHA sensor that dominates its optical response to refractive index changes.[12] Simple mass transport analyses have shown that the probability of a given molecule finding its way to the active site of the sensor in a reasonable time is virtually zero in any common configuration.[13,14] Therefore, directed transport of analytes or biomolecules is required to increase the sensitivity of nanoscale sensors. This has already been demonstrated by using flow-through configurations,[15,16]

Received: October 6, 2022
Accepted: November 11, 2022
Published: November 22, 2022

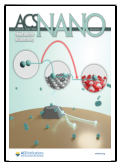

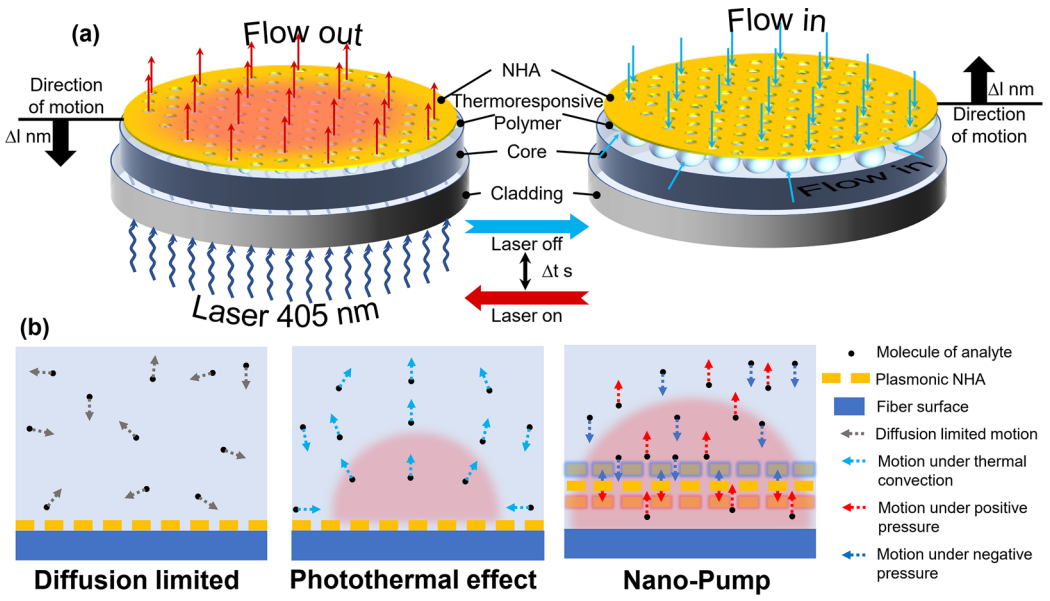

Figure 1. Photothermomechanical (PTM) nanopump (NP). (a) Visual representation of the PTM pump in action. The gold nanohole array (NHA) and the thermoresponsive polymer, i.e. polyNIPAM, are the key components. In the presence of laser light of 405 nm, heat is generated in the NHA due to the photothermal effect, which leads to the release of water from the polyNIPAM monolayer (collapse). The water release (flow-out) is maximum when the generated temperature exceeds the volume phase transition temperature (VPTT, the temperature at which the thermoresponsive polymer undergoes a phase transition) of the polyNIPAM. When the laser is turned off, the temperature drops below the VPTT of polyNIPAM, causing the polymer to take up water and swell to its original shape, causing a water influx (flow-in). The "laser off" and "laser on" sequence can be repeated to create a mechanical pumping motion that results in flow. (b) Pictorial representation of mass transport in diffusion vs photothermal effect/thermoplasmonics vs PTM pumping scenarios. The PTM pumping has the advantage of flow-through operation and is therefore more sensitive than the others.

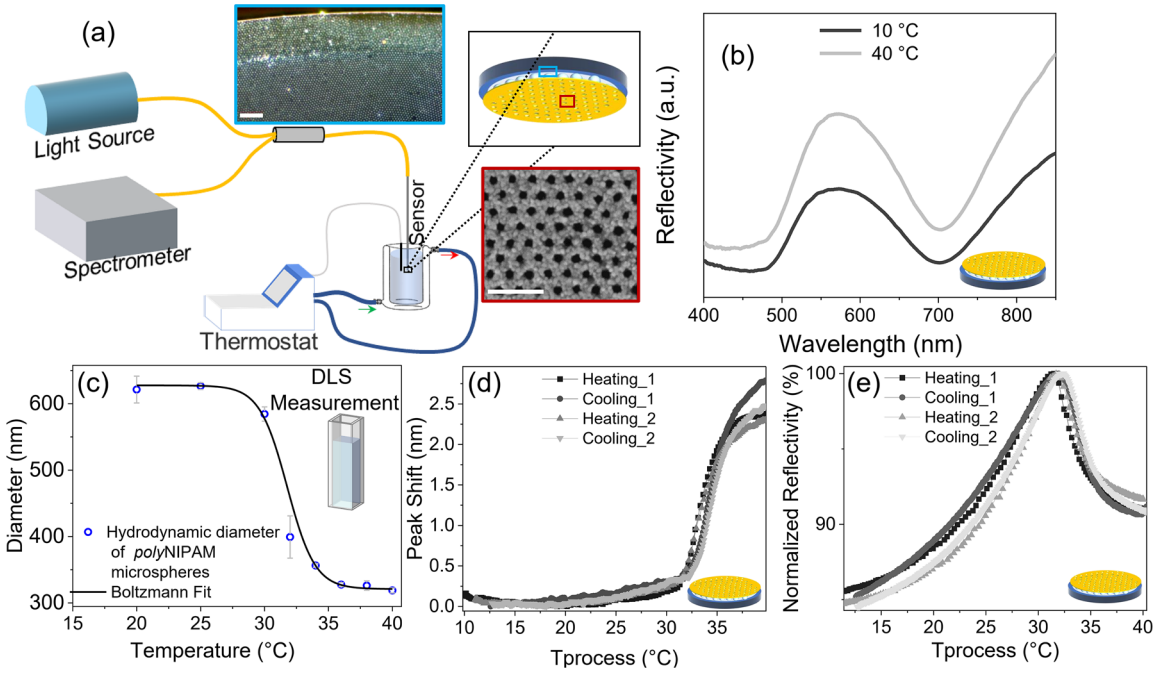

Figure 2. Characterization of NP. (a) Instrumentation: instrumental setup to perform spectroscopic analysis with representative polyNIPAM monolayer on the blue box (scale bar 10 mm) and NHA red box (scale 1 mm), (b) Reflectance spectra of the NP in the geometry shown in (a) at 10 °C and 40 °C, (c) DLS Measurements: Change in diameter of polyNIPAM microspheres in water dispersion as a function of temperature. (d) and (e) show changes in peak position (peak shift) and normalized reflectivity as a function of temperature for different cycles, respectively.

thermal convection,[17] electrophoresis,[18] dielectrophoresis,[19] and electro-osmosis.[20]

A particularly intriguing approach is the dual use of an NHA sensor for both signal transmission and heat generation to induce flow toward the nanoholes. Heat can be efficiently generated in the NHAs by irradiation with light of suitable wavelength.[21,22] Through the resulting so-called photothermal effect, convective flow through the NHAs has already been described, although the complexity of thermally driven fluid dynamic phenomena limits its applicability. However, all

https://doi.org/10.1021/acsnano.2c09938
ACS Nano 2023, 17, 1403−1413

previous reports on sensors based on NHAs in combination with optical fibers refer to dead ends on operating in flow-over mode.

In this work, we report a light-driven mechanical nanopump (NP) on an optical fiber tip designed for active transport of target analytes to the sensor. Here, signal detection and illumination for photothermal heat generation, which drives the NP, occur simultaneously. To this end, we coated an optical fiber tip successively with stimuli-responsive hydrogel microgels and with an NHA. The temperature-dependent collapse and swelling of the hydrogel microgel, driven by heat generation in the NHA mediated by the photothermal effect upon illumination, is used to create a flow pump mechanism. Finally, we demonstrate the performance of the nanopump by studying the active mass transport through the NHA of spherical gold nanoparticles as a nanoscale model object and 11-mercaptoundecanoic acid (MUA) as a model analyte.

RESULTS AND DISCUSSION

The working principle of the mechanical effect of the photothermomechanical nanopump (PTM-NP) is shown in Figure 1.

Upon laser illumination, the NHA layer is photothermally heated above the volume phase transition temperature (VPTT, the temperature at which the thermoresponsive polymer undergoes a phase transition) of polyNIPAM, causing the thermoresponsive polymer to collapse and the medium to be released into the environment through the nanoholes. The direction of motion for the NHA is downward (Δl), while the flow is always forward due to the gradient created by the pumping motion generation. In the absence of the laser, the NHA and the polyNIPAM monolayer cool rapidly, causing the polymer to expand (swell) and creating a negative pressure between the NHA layer and the fiber tip. As a result, it sucks the medium including the analyte through the nanoholes (Figure 1). A continuous pumping sequence can thus be generated by several consecutive laser pulses (Δt, the time between two consecutive pulses).

Fabrication and Characterization of Photothermomechanical Nanopump. PTM-NPs were fabricated by depositing a loosely packed array of polyNIPAM microspheres and subsequently an NHA on top of an optical fiber tip. To apply the microgel to the optical fiber tip, a monolayer was self-assembled at an air−water interface and then transferred to the fiber tip. A dark-field microscopy image of such a polyNIPAM monolayer after deposition on the fiber tip is shown in Figure 2b as well as in Figure S4. From the image, it can be seen that the fiber surface including the core and cladding region is uniformly covered. The diameter of the polyNIPAM microspheres and the lattice constant of the array determined from several images ($n = 6$) as shown in Figure S4 are 734 ± 46 nm and 1033 ± 114 nm, respectively. The appearance of vivid coloration upon additional lateral illumination indicates the successful transfer of a uniform and ordered polyNIPAM monolayer onto the fiber tip (Figure S3d, insets).

NHAs used in this study were fabricated by a bottom-up method on a glass substrate and then transferred to the fiber tip using a strategy described in previous publications.[11,23] A representative SEM image of an NHA is shown in Figure 2b. The detailed size distribution and lattice constant were calculated based on images captured across three batches ($n = 9$) with at least three samples from each batch and are shown in Figure S1. It was found that the diameter of the holes is 161 nm, with a standard deviation of 13 nm. The lattice constant of the NHA used in our study is about 378 nm (Figure S1), calculated from the radial distribution function[24] of the holes shown in Figure S1. The thickness of the NHA gold film is 68 ± 9 nm ($n = 3$) and was determined by atomic force microscopy (AFM) on three different samples (Figure S2).

The PTM-NP geometry was constructed by introducing NHA on top of a polyNIPAM monolayer at the tip of an optical fiber. NHA applied directly to the fiber tip, without the thermoresponsive polymer, served as a reference for further experiments in this study. The fabrication protocol for both sensor types is summarized pictorially in Figure S5. The SEM images of a damaged NP sensor shown in Figure S6 confirm the successful formation of the PTM-NP geometry. The polyNIPAM microspheres are visible on the lifted and inverted NHA surface. To investigate the effect of the polyNIPAM monolayer on the plasmonic response of the NHA in NP geometry, reflectance spectroscopy was performed. The plasmonic peak positions obtained from the reflectance spectra of bare NHA and PTM-NP in air for five different sensors are summarized in Table S1. The peak position of bare NHA is at a wavelength of 604 ± 15 nm ($n = 5$), while the plasmonic peak position of PTM-NP is 611 ± 21 nm ($n = 5$). The presence of a polyNIPAM monolayer under the NHA for the PTM-NP geometry is the reason for the red-shifted plasmonic peak position with respect to NHA alone. It is worth mentioning that the position of the plasmonic peak in the NP depends on the state of the polyNIPAM monolayer, which is determined by the environmental conditions (temperature, humidity). Thus, the red shift of the plasmonic peak for PTM-NP in comparison to bare NHA, both detected in air, can be attributed to the change in the refractive index in close proximity to the sensor surface of the NHA due to the presence of an additional polyNIPAM layer with a higher refractive index than air in the PTM-NP geometry.

Response toward External Thermal Stimuli. Figure 2a shows the experimental setup to study the optical response of the PTM-NP to external temperature stimuli. The NPs were immersed in water in a jacketed beaker with stirring, and the temperature of the beaker was controlled externally by a thermostat. The temperature of the water was monitored with a thermocouple near the NP sensor. The optical responses in reflectance mode of an NP at 10 and 40 °C are shown in Figure 2b. From the reflection spectra at 10 and 40 °C, the change in the position of the plasmonic peak and the reflection amplitude can be seen. The change of the local RI in the vicinity of the NHA is directly related to the position of the plasmonic peak of the sensor. In the case of the NP the NHA is deposited onto a layer of a polyNIPAM microgel, which swells and collapses by intake and release of water and thereby changes its size and refractive index.[25] The thermoresponsive properties of polyNIPAM are evident from the temperature-dependent DLS measurements (Figure 2c). The hydrodynamic diameter of the polyNIPAM microgel sphere changes from 621 ± 20 nm (swollen) to 319 ± 4 nm (collapsed) when the temperature is increased from 20 to 40 °C. The so-called volume phase transition temperature (VPTT), at which the particles collapse due to changes in the hydrophilicity of the polyNIPAM and most of the previously stored water is released, was determined to be 31.78 °C (~32 °C) using a Boltzmann fit (D50 value). By decreasing the temperature below the VPTT, the hydrophilicity changes again and the particles start to restore water and reach the swollen state. This process is completely reversible.[26] The polyNIPAM has a refractive index (RI) of 1.36 at room temperature (22 °C) in water and of to 1.46 at 40 °C,[27] leading

https://doi.org/10.1021/acsnano.2c09938
ACS Nano 2023, 17, 1403−1413

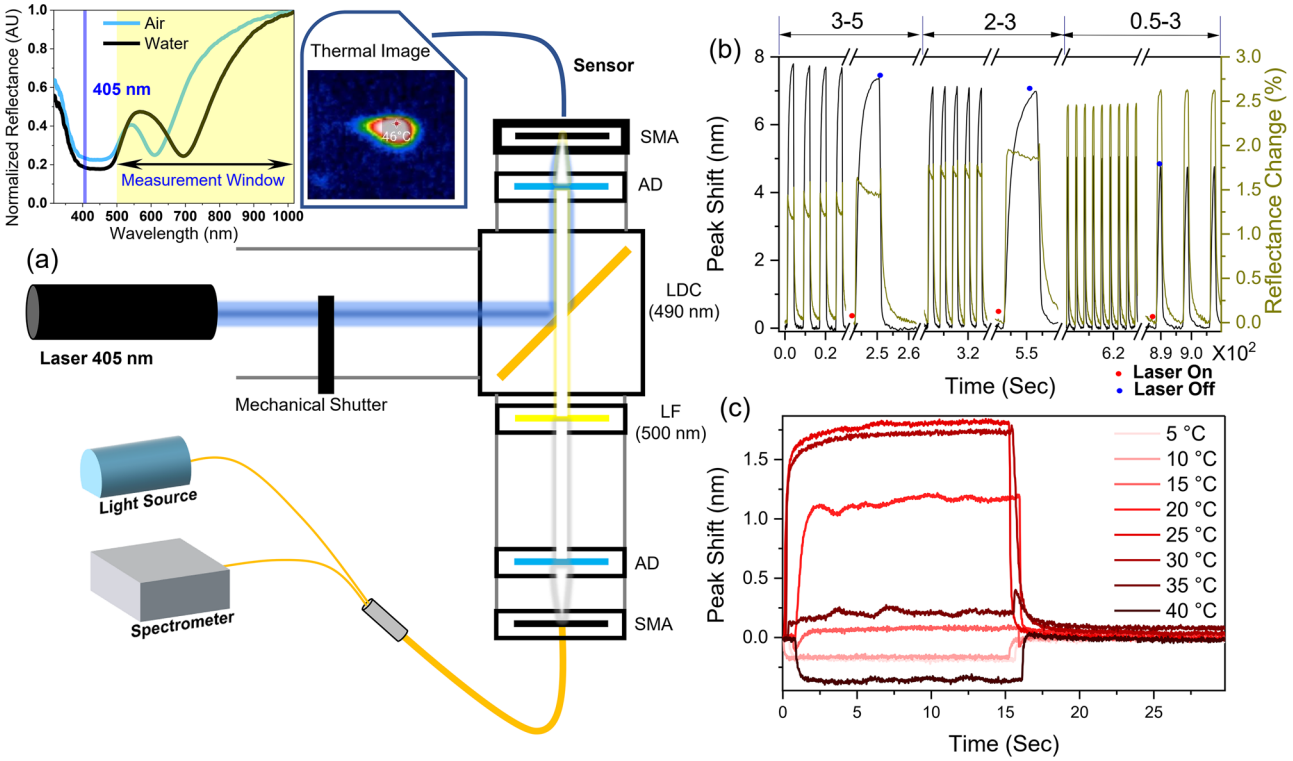

Figure 3. Instrumentation and proof of concept. (a) Instrument setup to perform photothermal excitation and spectroscopic analysis simultaneously (SMA, subminiature A connector; AD, achromatic doublet; LF, long-pass filter; LDC, dichroic long-pass mirror). Inset: selection of laser wavelength (blue line) and measurement window (highlighted in yellow) and representative thermal image of NP in the steady state, with CW laser exposure at 405 nm. (b) Plasmonic response of NHA onto NP when immersed in water with different laser pulse durations (duty cycle off-duration: 3−5, 2−3, 0.5−3). (c) Effect of external temperature onto the plasmonic response of NHA to NP (15−15).

to the observed red shift of the spectral position of the plasmonic peak.

The observed increase in reflection amplitude is mainly determined by the change in the distance between the fiber and the NHA in the NP sensor due to the collapse of polyNIPAM at 40 °C. In addition, the scattering contributions and Fresnel reflectances at 10 and 40 °C differ due to the different RI values of polyNIPAM in the swollen and collapsed states: i.e., the degree of swelling of the polyNIPAM layer located between the optical fiber tip and the NHA determines its refractive index and thereby the measured reflectance.

To investigate the dynamics of the NP sensor with temperature, a temperature ramp experiment was performed in the temperature range from 10 to 40 °C. The ramp consisted of two consecutive heating and cooling cycles: namely, Heating_1, Cooling_1, Heating_2, and Cooling_2. The changes in plasmonic peak position and reflectance were tracked throughout the experiment using a custom-written MATLAB code (Materials and Methods) and are shown in Figure 2d,e, respectively. The discussion on shift and change in amplitude of the plasmon peak is as follows

(i) Plasmon peak shift: the average change in plasmon peak shift for NP is about 2.25 ± 0.53 nm with a temperature change from 10 to 40 °C (Figure 2d). With an increase in temperature, the polyNIPAM starts to release water and the effective refractive index also increases, leading to a further red shift of the plasmonic peak of the NHA on the NP monolayer. The change is abrupt at a temperature of around 32 °C, the VPTT of polyNIPAM, in accordance with dynamic light scattering measurements shown in Figure 2c. It is worth noting that the polyNIPAM monolayer is not a continuous film but a combination of microspheres and water (Figure S7). Therefore, the effective change in RI is less than that of a closed polyNIPAM film. Moreover, in the case of the NP geometry only one side of the NHA is covered with the polyNIPAM monolayer while the other side is solely exposed to the surrounding medium water. Water has a negative thermo-optic coefficient, i.e., the RI of water decreases with increasing temperature (Figure S8, which also means that a blue shift of the plasmonic band is expected for NHA alone), while it is the opposite for polyNIPAM. The overall plasmonic response of NHA geometry upon temperature change is therefore overwhelmingly dominated by water. The positive thermo-optic coefficient of the polyNIPAM monolayer leads to a red shift of the plasmonic peak minima with minimal contribution to the effective shift of the plasmonic response of NHA on the NP.

(ii) Plasmon peak amplitude: the kinetic response of the reflectivity at plasmon peak minima as a function of ambient temperature is shown in Figure 2e. As the temperature is increased, the polyNIPAM releases water and collapses. The distance between the fiber surface and the NHA in the NP sensor also decreases, as shown in the AFM study (Figure S7). The shortening of the distance between the fiber and the reflective NHA further increases the reflectivity. The change in RI of polyNIPAM as a function of temperature also has an additive effect on the reflectance value: as the temperature increases, the RI increases and so does the reflectance. The sharp increase

https://doi.org/10.1021/acsnano.2c09938
ACS Nano 2023, 17, 1403−1413

and decrease in reflectance at about 32 °C indicates the VPTT temperature of polyNIPAM, which is known and has been reported in the literature.[28]

Photothermal Effect. For this study, a continuous wave (CW) diode laser with a wavelength of 405 nm was chosen. Since this is above the plasma frequency of gold, the heat generated is solely due to electron interband transitions and subsequent radiation-free relaxation in the gold atoms, which is known as the photothermal effect.[29] Comparatively simpler instrumentation was required for the laser in the blue region (Figure 3a) than in the plasmonic region. While a wavelength of 405 nm was used to generate heat due to the photothermal effect, the plasmonic response of NHA (500−700 nm) can be used for simultaneous sensing applications (Figure 3a, left panel). The heat generated by the photothermal effect in the NP sensor was monitored using a thermal imaging camera with continuous exposure for 50 s. The temperature reaches a constant value within 10−12 s after exposure. For comparison, the heat generated in the NHA was also monitored. Constant temperature values of 42 °C for NP and 43.66 °C for NHA were observed when three sensors of each type were measured (Figure S10). A representative thermal image of the NP sensor is also shown in Figure 3a (left part). It should be noted that the thermal imaging camera used for this study is not very accurate for recording the temperature of an object with a size of 1 mm.[30] Based on the simulation study, the predicted temperature of the film under laser irradiation can reach up to ∼59 °C, as shown in Figure S11. No significant difference in temperature was found for NP and NHA. Thus, a temperature higher than the VPTT of the polyNIPAM can be achieved with laser irradiation (66 mW) at the sensors with a power density of 84 kW/m^2.

Photothermomechanical (PTM) Pumping. To exploit the photothermal excitation of the NHA for pumping and simultaneously monitoring changes in the optical response of the NHA, the previously described optical setup (Figure 1b) was adapted. Here, coupling of the 405 nm "excitation" laser to a mechanical shutter allows for controlling the on−off duration of the laser (Figure 3a). The kinetic response of the plasmonic minima of the NP sensor when it is immersed in static water is shown in Figure 3b. The position of the plasmonic peaks and the reflectivity were determined using a custom MATLAB code (Materials and Methods). Three different on−off cycles with durations of 3−5, 2−3, and 0.5−3 are highlighted in the graph. Two types of observations can be made based on the graph shown.

(i) Plasmonic peak shift: regardless of the cycle type, a plasmonic red shift is observed when the laser is turned on, while it returns to its original state when the laser is turned off. This scenario is similar to the observation shown in Figure 2d, but in this case, the temperature generation is in the sensor itself (photothermal effect of NHA). On the other hand, if we perform the same experiment with NHA alone, we obtain a blue shift of the plasmonic minima (Figure S12). This is because, as the local temperature changes due to the photothermal effect, the RI of water decreases (an increase in temperature decreases the RI of water; Figure S8), causing the plasmonic peak to shift to the blue. In the case of NP, a maximum plasmonic peak shift of 8 nm can be observed during the 3−5 s cycle at the onset of the laser. The peak shift decreases by almost 0.6 nm in cycles 2 and 3, which could be related to the shorter exposure time. A minimum peak shift of about 5 nm can be observed at a cycle of 0.5−3. We will explore the reasons for this in the following section with a more detailed analysis.

(ii) Change in reflectivity: in the reflectivity data, the sharp hump at the beginning and end of the pulse is characteristic of polyNIPAM, which is consistent with the data shown in Figure 2e, indicating that the temperature exceeds the VPTT of polyNIPAM in the case of 3−5 and 2−3 cycles. However, this is not the case in the 0.5−3 cycle. This indicates that the duty cycle at the given laser power density is not sufficient to exceed the VPTT of polyNIPAM. The increase in reflectance with each cycle is not yet fully understood.

To further substantiate the mechanism of PTM-NP, a pumping experiment was performed with a fixed duration of 15−15 s (15 s on and 15 s off) under different external temperature conditions (5, 10, 15, 20, 25, 30, 35, and 40 °C). In this case, the NP sensor was immersed in water and kept in a jacketed beaker under stirring (to distribute the heat uniformly), the temperature of which was controlled by a thermostat (see Figure 2b). The kinetics of 10 consecutive pump cycles for each temperature are shown in Figure S13. The plasmonic peak shift of the cycle (number one) corresponding to each temperature is shown in Figure 3c. The negative peak shift (blue shift) at temperatures of 5 and 10 °C shows that the heat generated by the photothermal effect is not able to induce significant changes on the polyNIPAM microspheres. The shift of the plasmonic peak is dominated only by the effect of water, as shown by the observations made for NHA alone (Figure S12). With increasing temperature, the peak shift reaches its maximum at 25 °C and decreases at 35 °C and has a negative value at 40 °C. When the ambient temperature is increased from 15 to 30 °C, the contribution of polyNIPAM becomes dominant compared to that of water, resulting in a positive peak shift. However, at 35 and 40 °C, the polyNIPAM microspheres are already in the collapsed state, and a further temperature increase does not lead to any changes in their structure. Therefore, as in the case of NHA, the peak shift is dominated only by water (Figure S12). Further conclusive evidence can be obtained from the reflectance data at 30 °C. The characteristic humps at the beginning and end of the pulse indicate the VPTT of polyNIPAM.

The temporal response of pumping (laser on) and regenerating (laser off) depends on many factors, including sample volume, vessel geometry, sample temperature, and conditions (Figure S14). The plasmonic response of NP under different conditions (volume, conditions) is shown in Figure S13. For water with volumes of 1000 and 100 mL, a time component of about 532 ms was observed when the laser of NP was applied. However, for water under stirring conditions, the trend is more complex, while for water kept in a capillary with a volume of less than 1 mL, a time component of 320 ms is observed. The regeneration time constant (laser off) was found to be about 72 ms. A complete understanding is beyond the scope of the present study. However, for the given laser wavelength and power density in still water, the minimum time between subsequent pumping events (Δt) should be around 600 ms.

Advantage of PTM Pumping over Convection. To evaluate the advantage of pumping over convection due to the photothermal effect, particle imaging velocimetry (PIV) was performed for NHA alone and NP using the MATLAB tool

https://doi.org/10.1021/acsnano.2c09938
ACS Nano 2023, 17, 1403−1413

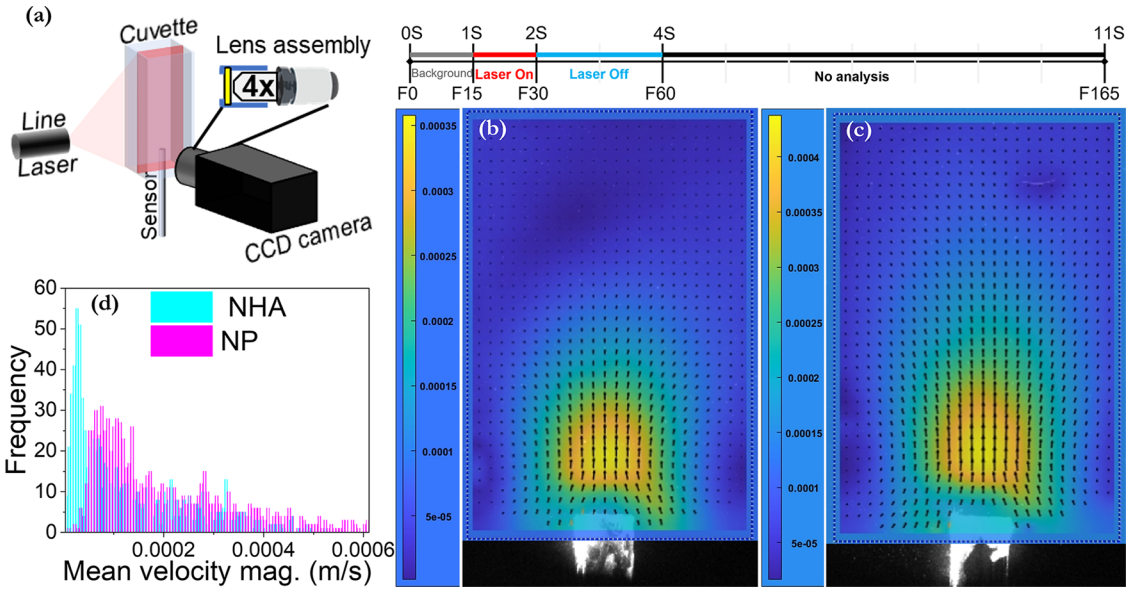

Figure 4. Advantage of PTM pumping over convection. (a) Schematic of the optical setup used to perform particle imaging velocimetry (PIV) experiments. A red line laser is used to generate an arc in the cuvette containing polystyrene (PS) particles suspended in water, with a sensor in the center. A CCD camera with a lens assembly (500 nm long-pass filter → 4× lens → videography lens) was used to film the light sheet at a frame (F) rate of 15 F/sec. An overall schematic of the 1−10 laser sequence used for the pump experiment is shown at the top right. The mean velocity maps as obtained by a PIV analysis from F16 (laser on) to F60 (end of experiment) for NHA (b) and NP (c) are shown. The histogram of the velocity component from (b) and (c) shows a mean particle velocity of 0.53 mm/s for the NHA and 0.83 mm/s for the NP geometry.

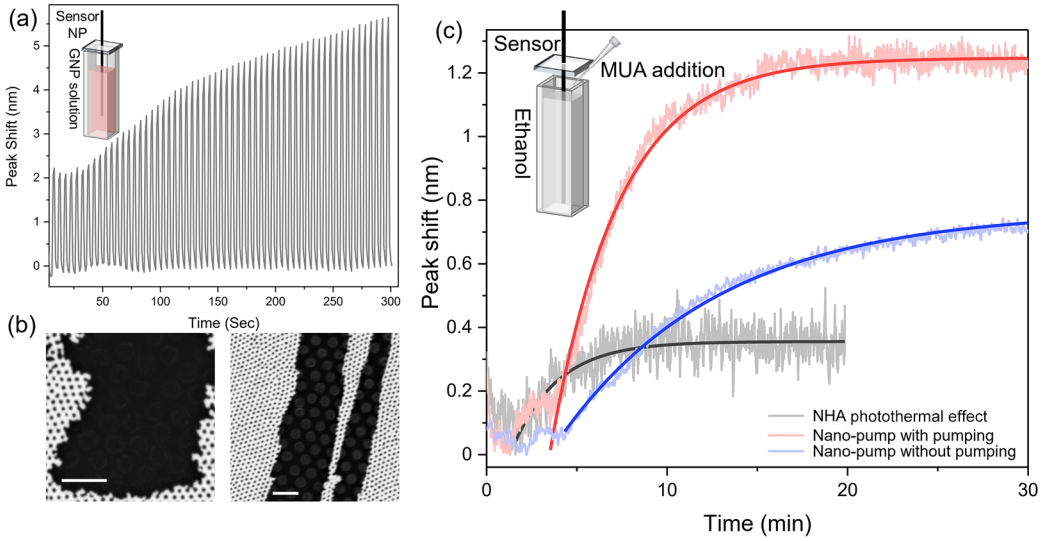

Figure 5. Advantage of the NP in sensing. (a) Active mass transport through holes in NP using gold nanoparticles (GNP) as model analytes. The NP sensor was operated with two to three laser pulses while it was immersed in a GNP solution. (b) SEM images of the manipulated NP after previous experiments under the same recording conditions (10 kV), (left) with GNP in low concentration (strain/10) and (right) high concentration (strain) GNP (scale bar 2 μm). (c) Comparative surface adsorption study of the conventional photothermal effect in NHA (gray) with NP geometry in the presence (red) and absence (blue) of pumping motion with MUA as a model analyte. A steady-state peak shift of 1.17 nm is obtained for NP with pump motion in contrast to 0.35 nm for NHA with pump motion. The NHA leads to a characteristic time constant of 2.48 min compared to 4.70 min for the NP geometry with pumping motion and 8.86 min without pumping motion.

PIVlab. The basic optical setup for recording time-lapse videos of polystyrene (PS) particle motion (suspended PS particles in water) in vertical geometry is shown in Figure 4a. The laser sequence chosen for this study was 1−10 with three consecutive repetition cycles. The choice of a laser duration of 1 s is based on the observation that the temperature generated in NHA is just sufficient to exceed the VPTT of polyNIPAM. Dynamic motion of the liquid due to the photothermal effect could dominate over pumping if the on duration is longer than 1 s. A laser-off duration of 10 s is sufficient to allow the flow generated by pumping to decay. Video curves recorded at a frame rate of 15 frames (F) per second (F/s) for NHA and NP alone are shown in the Supporting Information (NHA_P1_SV1, NHA_P2_SV2, NP_P1_SV3, and NP_P2_SV4 for two consecutive pulses). The average velocity amplitudes obtained from a PIV analysis from F16 to F60 (laser off at F30) of the NHA and NP structures are shown in Figure 4b,c, respectively. Figure 4d shows a histogram of velocity amplitudes for each geometry type with a

https://doi.org/10.1021/acsnano.2c09938
ACS Nano 2023, 17, 1403−1413

mean velocity of 0.53 mm/s for NHA and 0.83 mm/s for NP. Thus, a factor of 1.52 is obtained in the average velocity versus convection alone. In reproducibility experiments, the value was found to vary between 1.4 and 2.2. The average velocity corresponding to an area of 2.4706×10^{-6} m^2 from each frame over three consecutive cycles for NHA and NP is shown in Figure S15. A higher average velocity of 0.33 mm/s was obtained with NP at F60 of the pulse (number one), compared with 0.239 mm/s for NHA.

Advantage of NP in Flow-Through Sensing. We have provided experimental evidence of active mass transport through nanoholes in our NP. A suspension of gold nanoparticles (GNP) (~10 nm) was used as model analytes under two to three laser sequences over 5 min. The plasmonic peak shift kinetic data are shown in Figure S16, while the baseline-subtracted data are shown in Figure 5a. Two observations can be derived from the experimental data. At the beginning, the increase in the red shift of the plasmonic peak position (baseline drift) and the increase in the plasmonic peak shift are due to the pumping motion with time (Figure 5a). Both observations are associated with the incorporation of GNPs into the polyNIPAM microspheres. With each pumping step, the loading of GNPs into the polyNIPAM increases and so does the effective RI of the polyNIPAM monolayer. Consequently, the peak shift also increases with time at each pumping cycle. The overall baseline shift indicates the loading rate of GNPs into the polyNIPAM. As further evidence of the mechanism, SEM images taken under similar imaging conditions of two mechanically manipulated/damaged probes after the low-concentration (stock/10) and high-concentration (stock) pumping experiments are shown on the left and right in Figure 5b, respectively. The stronger contrast in visibility of the polyNIPAM microspheres under the NHA in Figure 5b on the right compared to the left is directly related to the incorporation of GNP into the polyNIPAM microspheres.

To evaluate the efficacy of NP for sensing applications, we investigated the formation of a self-assembled monolayer (SAM) of 11-mercaptoundecanoic acid (MUA) on the NHA surface in terms of plasmonic tip displacement, as described by Eftekhari et al.[31] MUA with a concentration of 1.25 μM in ethanol is considered as an analyte in this study. The laser power used in this particular study was reduced to half (~30 mW) to consider a real application scenario: i.e., the temperature generated by the photothermal effect should be minimal. Three different scenarios are considered for this comparative study. The NP structure with pumping mechanism (Figure 5c, red) and without pumping mechanism (Figure 5c, blue) are the main conditions for this study. To evaluate the contribution of convection only due to the photothermal effect, the response of the sensor with NHA is also performed under similar experimental conditions (Figure 5c, gray). The time constants, obtained upon mathematical fitting by a first-order exponential function ($y = A_1 * \exp(-x/t_1) + y_0$), for NP with pumping (laser in use) are 3.8 and 5.6 min, while without pumping (laser not in use) they are 11.00 and 8.8 min for two different series of measurements (Table S2). Average peak shifts of 1.2 and 0.9 nm are obtained for the NP with and without pumping, respectively. Since the photothermal effect generates a convection current that internally accelerates the SAM formation of MUA, the time constant for NHA is 2.5 min with a peak shift of 0.36 nm. It is worth noting that the peak shift for NHA in the scenario with NP control (no pumping) is almost half. This observation could be related to the fact that the suspended NHA in the NP structure can accommodate twice as many molecules on the surface. The time constant with pumping sequence is faster for both NP and NHA compared to NP without pumping. However, the sensitivity is 4 times higher for NP than for NHA. Therefore, the proof-of-concept demonstration of our NP shows improved performance in sensing applications. In this regard, the volume outflow of the PTM-NP would also play an important role in the sensor performance of the PTM-NP. To determine this value, AFM measurements were performed in tapping mode on polyNIPAM monolayers in both dry and wet states. Here, the polyNIPAM monolayer under water mimics the shape of polyNIPAM in the swollen state (at room temperature, i.e., ~20 °C), while the polyNIPAM in air represents the collapsed state (temperature >VPTT: i.e., above 32 °C). The AFM data obtained in both scenarios are shown in Figure S7. The average heights h under water and in air are 119 ± 13 nm and 46 ± 3 nm, respectively, which corresponds to a decrease of more than 60% in height (73 nm) in the collapsed state compared to the swollen state. In this case, a volume outflow of ~57 picoliters (pL) is expected for the NHA covering the entire end facet of the fiber in a single transition from the swollen state to the collapsed state of polyNIPAM in the NP, where the diameter of the fiber tip is 1000 μm. This volume appears to be relatively small but can easily be increased significantly by pumping. In general, miniaturized sensors have the problem that target analytes must be directed to small sensor areas, which could limit their range of application to small sample volumes. In the presented PTM-NP, the minimum time between successive pumping events is in the millisecond range, as mentioned earlier, which allows efficient transport of analytes from the sample to the sensor surface in a reasonable time. It should be mentioned that efficient transport has also been reported for surface-tension-induced passive flow through nanohole sensors.[32−34] Here, the pores in a thin, suspended nanopore array act as passive "nanodrains" that use capillary flow to accumulate analytes at the sensor surface. These sensors can be operated without an external pump or fluidic connections, making them simple, portable, and perfect for studying small-volume samples. However, compared to surface-tension-induced passive nanodrain sensors, the presented PTM-NP offers several advantages: a low-cost fabrication method, robust handling, and the implementation of real-time monitoring of binding events at the sensor surface.

CONCLUSIONS

In summary, a photothermomechanical nanopump (PTM-NP) on an optical fiber tip was presented which was fabricated using a pure bottom-up strategy. The PTM-NP consists of a monolayer of thermoresponsive polymer (polyNIPAM microgel particles) sandwiched between an optical fiber tip and a plasmonic nanohole array (NHA). The temperature-dependent collapse and swelling of the polyNIPAM particles was exploited for pumping by using the photothermal effect in the NHA upon illumination. The pumping contributes to more molecules reaching the sensor site, which means that a smaller number of molecules is required to generate a detectable signal. Active mass transport through the holes is expected to improve the sensitivity and detection limit and shorten the detection time. In addition, the plasmonic peak of the NHA was used to simultaneously detect the change in the refractive index of the environment. The flow-through NP concept has several advantages over conventional flow-over sensing strategies, including the fact that no separate pumping device is required,

https://doi.org/10.1021/acsnano.2c09938
ACS Nano 2023, 17, 1403−1413

the sample/reagent volume is minimal, and the sensitivity is high. The experimental setup presented for using the PTM-NP is already portable but could be further miniaturized by, for example, replacing the spectrometer with a laser diode operating at a wavelength between 500 and 700 nm to monitor the optical response of the sensor. The advantages of the pump mechanism in sensor applications were demonstrated, where a 4-fold increase in sensitivity was observed in the presence of the pump mechanism compared to the photothermal-only effect. In addition, real-time monitoring of the enrichment and binding of two different analyte types, namely nanosized objects in the form of gold nanoparticles and an MUA representative for small molecules, to the sensor was proven. The concept should be easily transferable to the detection of e.g. viruses, antibodies, or DNA, as the photothermal effect has already been exploited for drug delivery[35] and biosensing.[36] The precise control of light-driven pumping and simultaneous plasmonic signal detection make this strategy very attractive. It is expected that the PTM-NP will be useful for applications such as nanovalves and plasmonic reactors, bringing plasmonic point-of-care biosensing one step closer to reality.

MATERIALS AND METHODS

Characterization. *Atomic Force Microscopy (AFM).* A Bruker Multimode 8 AFM instrument (Billerica, Massachusetts, USA) was used to acquire AFM images to determine the thickness of the NHA (Figure S2) and to investigate the morphology of the polyNIPAM monolayer on a surface (Figure S7). Cantilevers for measurements were ScanAsyst Air with a resonance frequency of 70 kHz and a force constant of 0.4 N/m for dry conditions and ScanAsyst Fluid with a resonance frequency of 150 kHz and a force constant of 0.7 N/m for liquid conditions. All measurements were carried out with the ScanAsyst tapping mode. For liquid measurements, 20 μL of H_2O was dropped on the sample and the tip was completely immersed.

Scanning Electron Microscopy (SEM). A Quanta 250 electron microscope from FEI Deutschland GmbH (Frankfurt am Main, Germany) was used to characterize the fabricated NHA (Figure S1). SEM images of the damaged NP sensor (Figure S6) were acquired using a Zeiss SEM (Gemini ultra plus model) at an accelerating voltage of 3 kV with an InLens detector.

Dynamic Light Scattering (DLS). DLS experiments were performed using a Zetasizer Ultra instrument from Malvern Panalytical Ltd. (Malvern, United Kingdom).

Preparation of NHA and NP Sensors. Optical fibers (JTFLH100010351400) from Laser Components GmbH (Olching, Germany) were used as sensor fibers for this study. The preparation process for NHA[11] and NP[23] sensors is described in detail in previous reports. Optical fibers were cleaved and polished to a length of ∼14 cm (NOVA NV-100 manufacturer, Krell Technologies Inc. New Jersey, United States; supplier, AMS Technologies AG, Martinsried, Germany), and one end of the fiber was immersed in a piranha solution (3:1 concentrated H_2SO_4 (96%) (Sigma-Aldrich):H_2O_2 (30%) (Merck KGaA), v:v; note that piranha solution is explosive and can cause severe skin burns) overnight. The fibers were then thoroughly rinsed with ultrapure water (Milli-Q Integral System, Merck Chemicals GmbH, Germany) and used for the further preparation process. In parallel, a self-supporting NHA-Au film and a highly ordered polyNIPAM microgel monolayer were prepared at the air−water interface in two separate beakers.[19] The NHA sensor was fabricated by functionalizing the clean end of the fiber with 3-aminopropyltriethoxysilane and then transferring the NHA to the fiber tip by dip coating. Another heat treatment step was performed in a hot air oven (Thermo Scientific Heraeus Function Line 110 L) at 80 °C for 1 h to ensure a strong bond between the gold and the fiber surface via the amino group of the silane molecule. The NP sensor was fabricated by transferring the polyNIPAM monolayer to the fiber tip by dip coating and then depositing the NHA on top.[23] The NP sensor was dried at room temperature for further experiments.

Reflectance Spectroscopy Setup. A fiber-based reflectance spectroscopy setup was used to record the plasmonic response of the sensors in air and to study the effects of external temperature on the sensors (see Figure 2b). An optical fiber bundle from Loptek GmbH (Berlin, Germany) with a core diameter of 100 μm per fiber was connected with an Ocean Optics HL-2000 light source and an Ocean Optics QE65 Pro spectrometer (OceanOptics BV, Ostfildern, Germany). Reflectance spectra were recorded using OceanView software on a laptop while the sensor was connected to the other end of the fiber bundle via an SMA-to-SMA connector. The spectra were recorded with an integration time of 33 ms and a mean scan of 5, using the reflectance of a bare fiber as a reference. The reflectance spectra of an NHA sensor recorded in air and water are shown as an inset in Figure 3a. To monitor the effect of temperature on the plasmonic response of the sensors, a thermostat (Huber ministate 230, PeterHuber Kältemaschinenbau AG, Offenburg, Germany) connected to a jacketed beaker containing 300 mL of Milli-Q water (volume 1000 mL, SCHOTT DURAN) was used with stirring (100 rpm). A temperature range of 10−42 °C was selected for this study. The sensor was immersed in water while a temperature sensor connected to the thermostat was placed nearby to monitor the temperature accurately. Both temperature values and reflectance spectra were recorded with a time interval of 5 s.

Determination of Reflectance Minima. To better track the plasmonic minima during the experiments, a Matlab-based program was used. Briefly, the position of the plasmonic minima in each recorded reflectance spectrum was determined by a fitting routine. The routine determined at the beginning the absolute minimum. This minimum was taken as the starting point. Then 256 data points of the experimental spectra surrounding this minimum were selected, and these points were fitted with the Matlab function polyfit with a degree of $n = 5$ ($f(x) = p_1x^5 + p_2x^4 + p_3x^3 + p_4x^2 + p_5x + p_6$). Searching for total minima in a region is more consistent than searching for a single minimum from the raw data to avoid noise. Apart from this, the fitting routine is required for a statistical treatment of large data sets.

Pumping Setup. The setup used for the pump study is an extension of a previous setup with the ability to couple blue laser light into the sensor. A 30 mm cage system (Thorlabs) was used for light management, shown schematically in Figure 3a. In the middle was placed a 30 mm Cage Cube (CM1-DCH) containing a Longpass Dichroic Mirror (LDC) and 490 nm Cut-On (Thorlabs DMLP490R). Two identical arms extending in opposite directions and containing an achromatic doublet (AD) (Thorlabs AC254−030-AB-ML; f = 30.0 mm) and an SMA fiber adapter (Thorlabs SM1SMA) were built. A reflectance spectroscopy setup and a sensor were connected to both ends via SMA connectors. An additional-long pass filter (LF) (cut-on wavelength 500 nm; Thorlabs FEL0500 - Ø1″) was placed in the light path in front of the cage cube to prevent laser light from reaching the spectrometer. The laser used in this study was a continuous wave diode laser (model, Wal frontg7v1 msdeky; manufacturer, Walfront, Wuhan, China) with a laser wavelength of 405 nm. The measured wavelength with a stability measurement is shown in Figure S9. The reason for choosing 405 nm is the possibility to monitor reflection spectra without interruption (Figure 3a). The laser was mounted on a large kinematic V-clamp (Thorlabs KM200 V/M) with a servo motor (Tower Pro, microServo 9g, SG90) mounted in front of it to act as a mechanical shutter. A simple Arduino IDE-based program was used to block or open the laser path in the desired time period. The laser sequence was referred to as on-time−off-time in the manuscript: e.g., 2−3 (the laser path was opened for 2 s and closed for 3 s). The reflectance spectra in the pump setup were recorded using an Au film (thickness ∼70 nm) on a fiber as a reference in OceanView software with different data storage intervals according to the experimental requirements.

Thermal Imaging. The sensors (NHA/NP) were connected to the SMA connector of the pump assembly. A 405 nm laser was continuously shined, which further heated the fiber tip by the photothermal effect on the plasmonic NHA. A thermal imaging camera (Seek Thermal Compact Android IR camera, Conrad Electronic Se,

https://doi.org/10.1021/acsnano.2c09938
ACS Nano 2023, 17, 1403−1413

Hirschau, Germany) was placed ∼12 cm away from the fiber tip for thermography. Thermography was performed for 50 s, and the temperature of the tip reached a constant value within 10−12 s.

Simulation. The temperature profile of NHA upon laser irradiation due to the photothermal effect was calculated using the finite element method (FEM in the COMSOL Multiphysics software). The structure was simplified by restricting the calculation to a hexagonal unit cell with side lengths of 218 nm and applying periodic boundary conditions. The unit cell includes a 161 nm diameter hole in a 67 nm thick gold membrane sandwiched between a 0.1 mm thick water layer and a 0.1 mm thick fiber (for NHA). In the case of the NP sensor, a space of 100 nm filled with water between the fiber and the gold membrane was considered to account for the optical properties of polyNIPAM. All materials were modeled using data from the COMSOL materials library. For this purpose, the absorbed power was calculated. To do this, the power incident on the unit cell was calculated to a value in the range of 10 nW. This power was used to calculate the absorbed power density of the metal through a frequency domain study, where the field is excited by a periodic port boundary condition and the absorbed power is calculated as a function of position. Due to the high thermal conductivity of gold, the entire metal volume will heat rapidly, justifying the replacement of a position-dependent thermal density with a homogeneous heat source with an average thermal density. Integrating the absorbed power density across the metal yielded an absorption of 7 nW, resulting in an average absorbed power density on the order of 1 TW/m^3. This power density was then used as the heat source for a temperature calculation. The ends of the water and silica fiber layers were modeled using heat flux boundaries that define the heat exchange rate between the simulation region and a thermal bath at room temperature. Due to the long silica fiber and its aspect reatio, heat exchange on the silica site was believed to be negligible in comparison to the other loss channel and the heat exchange to this side was set to zero. On the water side, a typical value of 1000 W/(K m^2) was used.[37] The results of a steady-state calculation can be seen in Figure S11. The nonuniform temperature profile was mainly determined by the boundary conditions.

Particle Imaging Velocimetry Setup. To investigate the effects of pumping versus photothermal effect on fluid dynamics, 2 μm polystyrene microspheres (Polysciences, Inc. Polybead Sulfate 2.0 Micron Micro-Spheres (2.5% Solids-Latex)) were used as tracer particles. A schematic diagram of the experimental setup is shown in Figure 4a. A standard disposable cuvette (612-5503P, VWR International GmbH, Dresden, Germany) filled with a suspension of tracer particles in Milli-Q water was placed upside down in a custom 3D-printed platform capable of holding a sensor (NP/NHA) in the center. The platform was also mounted in a three-axis stage (Thorlabs NanoMax-TS). A focusable diode line laser with a wavelength of 650 nm (WYTP11-LA2, WayinTop, Guangdong Province, China) mounted on a small V-clamp (Thorlabs VC1/M) was placed on the cuvette to create a two-dimensional laser sheet. A camera (Point Gray: GRAS-20S4M-C, mono; 1624 × 1224) pointed perpendicular to the laser sheet was used to capture video images. To capture microscopic images and prevent the laser (405 nm) from reaching the camera, an optical assembly consisting of a long-pass filter (cut-on wavelength 500 nm; Thorlabs FEL0500 - Ø1″), an Olympus 4× lens (Thorlabs RMS4X-PF), and a Pentax TV lens (16 mm C-mount Pentax C1614-M lens) was used. The entire camera unit was placed using an optical stand on a linear translation stage (Thorlabs XR25C/M). The video was recorded using FlyCapture software with a resolution of 1600 × 1200 and a frame rate of 15 fps.

Particle Imaging Velocimetry. The velocity map and the average velocity presented in this article were calculated using PIVlab (version) developed for MATLAB.[38] PIVlab works on the basis of the statistical pattern matching technique. The recorded (or extracted from a video) image sequence was divided into subimages (query regions), and cross-correlation was performed for each of these subimages. The subsequent correlation matrix was used to determine the most likely displacement vector within each query region. The rate of the image sequence can also be used to determine the velocity component. The velocity vector field shown in Figure 4 was obtained by averaging over 45 images (F16−F60). The time-dependent (F1−F60) average velocity shown in Figure S15 was calculated for both geometries from a selected area of 2.47×10^{-6} m^2. Velocity distribution of particles for NHA only and NP obtained by the PIV analysis over the time window 0−4 s (F1−F60) for two consecutive laser pulses has been provided in supplementary videos (NHA_P1_SV1, NHA_P2_SV2, NP_P1_SV3, and NP_P2_SV4).

Flow-Through Sensing Setup and Scheme. The flow-through experiment on active mass transport with NP sensors was performed by immersion in 4 mL of a GNP solution (prepared by a modified Turkevich method with a particle size of ∼40 nm in water suspension) in a standard disposable cuvette (612-5503P, VWR International GmbH, Dresden, Germany). The spectral response of the NP sensor was recorded in the pump setup with 2−3 laser sequences over 5 min. The plasmonic minima corresponding to each recorded reflectance spectrum after processing with a user-defined MATLAB code are shown in Figure 5a and in the Figure S15 in the Supporting Information. The scanning electron microscopy (SEM) images in Figure 5b,c were acquired in the Phenom desktop SEM (Phenom ProX, Thermo Fischer Scientific). For the sensor experiment, 4 mL of ethanol (99.9%) was placed in a disposable cuvette (612-5503P, VWR International GmbH, Dresden, Germany). Then, the sensor was immersed in ethanol at a distance of 0.5 cm from the bottom of the cuvette. Then, 5 μL of 1 mM 11-mercaptoundecanoic acid (MUA) in ethanol was carefully added with a pipet. In both the active mass transport experiment and the sensing experiment, an additional cap was placed on the cuvette to reduce convection due to evaporation (Figure 5d).

Statistics and Data Presentation. Data presented in this article are rounded to the nearest whole number where appropriate. For repeated measurements, values are presented as mean ± standard deviation (SD) divided by the number of measurements in the parentheses: e.g., $n = 3$ (three measurements were made to obtain the value).

ASSOCIATED CONTENT

Supporting Information

The Supporting Information is available free of charge at https://pubs.acs.org/doi/10.1021/acsnano.2c09938.

Experimental details, characterization of polyNIPAM monolayer and plasmonic nanohole arrays (micrographs, hole diameter distribution, and radial distribution function), atomic force microscopy images of polyNIPAM arrays and plasmonic nanohole arrays on solid glass substrates, additional SEM images of plasmonic nanohole arrays on top of a polyNIPAM monolayer, refractive index measurements, laser characterization, thermographs of sensor tips, simulation details, further characterization of photothermal effect and pumping, including a graph of flow-through active mass transportation using gold nanoparticles (PDF)

Velocity distribution of particles for NHA only and NP obtained by the PIV analysis for NHA_P1_SV1 (AVI)

Velocity distribution of particles for NHA only and NP obtained by the PIV analysis for NHA_P1_SV2 (AVI)

Velocity distribution of particles for NHA only and NP obtained by the PIV analysis for NHA_P1_SV3 (AVI)

Velocity distribution of particles for NHA only and NP obtained by the PIV analysis for NHA_P1_SV4 (AVI)

AUTHOR INFORMATION

Corresponding Authors

Nabarun Polley − *University of Potsdam, Institute of Chemistry, Physical Chemistry−innoFSPEC and Institute of Chemistry, 14476 Potsdam, Germany;* Present Address: Adams

https://doi.org/10.1021/acsnano.2c09938
ACS Nano 2023, 17, 1403−1413

University, School of Engneering & Technology, 700 126 Kolkata, India; Email: nabapolley@uni-potsdam.de

Claudia Pacholski − *University of Potsdam, Institute of Chemistry, Physical Chemistry−innoFSPEC and Institute of Chemistry, 14476 Potsdam, Germany;* orcid.org/0000-0003-1620-5783; Email: cpachols@uni-potsdam.de

Authors

Samim Sardar − *Center for Nano Science and Technology@ PoliMi, Istituto Italiano di Tecnologia, 20133 Milan, Italy;* orcid.org/0000-0003-1783-6974

Peter Werner − *University of Potsdam, Institute of Chemistry, Physical Chemistry−innoFSPEC and Institute of Chemistry, 14476 Potsdam, Germany*

Ingo Gersonde − *University of Potsdam, Institute of Chemistry, Physical Chemistry−innoFSPEC, 14476 Potsdam, Germany*

Yuya Kanehira − *University of Potsdam, Institute of Chemistry, 14476 Potsdam, Germany*

Ilko Bald − *University of Potsdam, Institute of Chemistry, Physical Chemistry−innoFSPEC and Institute of Chemistry, 14476 Potsdam, Germany;* orcid.org/0000-0002-6683-5065

Daniel Repp − *Institute of Applied Physics, Abbe Center of Photonics, Friedrich Schiller University Jena, 07745 Jena, Germany*

Thomas Pertsch − *Institute of Applied Physics, Abbe Center of Photonics, Friedrich Schiller University Jena, 07745 Jena, Germany; Max Planck School of Photonics, 07745 Jena, Germany;* orcid.org/0000-0003-4889-0869

Complete contact information is available at: https://pubs.acs.org/10.1021/acsnano.2c09938

Notes

The authors declare no competing financial interest.

ACKNOWLEDGMENTS

This work was supported by the German Federal Ministry of Education and Research (BMBF, grant number 03Z22AN12). C.P. gratefully acknowledges funding from the Deutsche Forschungsgemeinschaft (DFG, German Research Foundation) - project number 426213922. Also, D.R. and T.P. gratefully acknowledge funding from the Deutsche Forschungsgemeinschaft (Project-ID 398816777 - SFB 1375 and Project-ID 390713860 - EXC 2051). We thank Dr. S. Basak for permission to use the MATLAB-based program to determine the reflectance minima.

REFERENCES

(1) Ahuja, S.; Kumar, M. S.; Nandeshwar, R.; Kondabagil, K.; Tallur, S. Longer Amplicons Provide Better Sensitivity for Electrochemical Sensing of Viral Nucleic Acid in Water Samples Using PCB Electrodes. *Sci. Rep.* **2022**, *12* (1), 8814.

(2) Han, H.; Sohn, B.; Choi, J.; Jeon, S. Recent Advances in Magnetic Nanoparticle-Based Microfluidic Devices for the Pretreatment of Pathogenic Bacteria. *Biomedical Engineering Letters* **2021**, *11* (4), 297−307.

(3) Hakkel, K. D.; Petruzzella, M.; Ou, F.; van Klinken, A.; Pagliano, F.; Liu, T.; van Veldhoven, R. P. J.; Fiore, A. Integrated Near-Infrared Spectral Sensing. *Nat. Commun.* **2022**, *13* (1), 103.

(4) Amalfitano, E.; Karlikow, M.; Norouzi, M.; Jaenes, K.; Cicek, S.; Masum, F.; Sadat Mousavi, P.; Guo, Y.; Tang, L.; Sydor, A.; Ma, D.; Pearson, J. D.; Trcka, D.; Pinette, M.; Ambagala, A.; Babiuk, S.; Pickering, B.; Wrana, J.; Bremner, R.; Mazzulli, T.; Sinton, D.; Brumell, J. H.; Green, A. A.; Pardee, K. A Glucose Meter Interface for Point-of-Care Gene Circuit-Based Diagnostics. *Nat. Commun.* **2021**, *12* (1), 724.

(5) Masson, J.-F. Portable and Field-Deployed Surface Plasmon Resonance and Plasmonic Sensors. *Analyst* **2020**, *145* (11), 3776−3800.

(6) Wang, P.; Nasir, M. E.; Krasavin, A. V.; Dickson, W.; Jiang, Y.; Zayats, A. V. Plasmonic Metamaterials for Nanochemistry and Sensing. *Acc. Chem. Res.* **2019**, *52* (11), 3018−3028.

(7) Ebbesen, T. W.; Lezec, H. J.; Ghaemi, H. F.; Thio, T.; Wolff, P. A. Extraordinary Optical Transmission through Sub-Wavelength Hole Arrays. *Nature* **1998**, *391* (6668), 667−669.

(8) Prasad, A.; Choi, J.; Jia, Z.; Park, S.; Gartia, M. R. Nanohole Array Plasmonic Biosensors: Emerging Point-of-Care Applications. *Biosens. Bioelectron.* **2019**, *130*, 185−203.

(9) Jia, P.; Yang, J. Integration of Large-Area Metallic Nanohole Arrays with Multimode Optical Fibers for Surface Plasmon Resonance Sensing. *Appl. Phys. Lett.* **2013**, *102* (24), 243107.

(10) Jia, P.; Yang, Z.; Yang, J.; Ebendorff-Heidepriem, H. Quasiperiodic Nanohole Arrays on Optical Fibers as Plasmonic Sensors: Fabrication and Sensitivity Determination. *ACS Sensors* **2016**, *1* (8), 1078−1083.

(11) Polley, N.; Basak, S.; Hass, R.; Pacholski, C. Fiber Optic Plasmonic Sensors: Providing Sensitive Biosensor Platforms with Minimal Lab Equipment. *Biosens. Bioelectron.* **2019**, *132*, 368−374.

(12) Ferreira, J.; Santos, M. J. L.; Rahman, M. M.; Brolo, A. G.; Gordon, R.; Sinton, D.; Girotto, E. M. Attomolar Protein Detection Using In-Hole Surface Plasmon Resonance. *J. Am. Chem. Soc.* **2009**, *131* (2), 436−437.

(13) Nair, P. R.; Alam, M. A. Performance Limits of Nanobiosensors. *Appl. Phys. Lett.* **2006**, *88* (23), 233120.

(14) Sheehan, P. E.; Whitman, L. J. Detection Limits for Nanoscale Biosensors. *Nano Lett.* **2005**, *5* (4), 803−807.

(15) Jonsson, M. P.; Dahlin, A. B.; Feuz, L.; Petronis, S.; Höök, F. Locally Functionalized Short-Range Ordered Nanoplasmonic Pores for Bioanalytical Sensing. *Anal. Chem.* **2010**, *82* (5), 2087−2094.

(16) Dahlin, A. B. Sensing Applications Based on Plasmonic Nanopores: The Hole Story. *Analyst* **2015**, *140* (14), 4748−4759.

(17) Garcia-Guirado, J.; Rica, R. A.; Ortega, J.; Medina, J.; Sanz, V.; Ruiz-Reina, E.; Quidant, R. Overcoming Diffusion-Limited Biosensing by Electrothermoplasmonics. *ACS Photonics* **2018**, *5*, 7.

(18) Zhang, J.; Wang, Y.; Wong, T. I.; Liu, X.; Zhou, X.; Liedberg, B. Electrofocusing-Enhanced Localized Surface Plasmon Resonance Biosensors. *Nanoscale* **2015**, *7* (41), 17244−17248.

(19) Barik, A.; Otto, L. M.; Yoo, D.; Jose, J.; Johnson, T. W.; Oh, S.-H. Dielectrophoresis-Enhanced Plasmonic Sensing with Gold Nanohole Arrays. *Nano Lett.* **2014**, *14* (4), 2006−2012.

(20) Song, Y.; Chen, P.; Chung, M. T.; Nidetz, R.; Park, Y.; Liu, Z.; McHugh, W.; Cornell, T. T.; Fu, J.; Kurabayashi, K. AC Electro-osmosis-Enhanced Nanoplasmofluidic Detection of Ultralow-Concentration Cytokine. *Nano Lett.* **2017**, *17* (4), 2374−2380.

(21) Tordera, D.; Zhao, D.; Volkov, A. V.; Crispin, X.; Jonsson, M. P. Thermoplasmonic Semitransparent Nanohole Electrodes. *Nano Lett.* **2017**, *17* (5), 3145−3151.

(22) Rogez, B.; Marmri, Z.; Thibaudau, F.; Baffou, G. Thermoplasmonics of Metal Layers and Nanoholes. *APL Photonics* **2021**, *6* (10), 101101.

(23) Polley, N.; Werner, P.; Balderas-Valadez, R. F.; Pacholski, C. Bottom, Top, or in Between: Combining Plasmonic Nanohole Arrays and Hydrogel Microgels for Optical Fiber Sensor Applications. *Advanced Materials Interfaces* **2022**, *9* (15), 2102312.

(24) Quint, S. B.; Pacholski, C. A Chemical Route to Sub-Wavelength Hole Arrays in Metallic Films. *J. Mater. Chem.* **2009**, *19* (33), 5906−5908.

(25) Jeenanong, A.; Kawaguchi, H. Effect of PH and Temperature on the Behavior of Microgel in SPR Sensor. *Colloids Surf., A* **2008**, *315* (1−3), 232−240.

(26) Pelton, R. H.; Chibante, P. Preparation of Aqueous Latices with N-Isopropylacrylamide. *Colloids Surf.* **1986**, *20* (3), 247−256.

(27) Sharma, N.; Keshmiri, H.; Zhou, X.; Wong, T. I.; Petri, C.; Jonas, U.; Liedberg, B.; Dostalek, J. Tunable Plasmonic Nanohole Arrays Actuated by a Thermoresponsive Hydrogel Cushion. *J. Phys. Chem. C* **2016**, *120* (1), 561−568.
(28) Werner, P.; Münzberg, M.; Hass, R.; Reich, O. Process Analytical Approaches for the Coil-to-Globule Transition of Poly(N-Isopropylacrylamide) in a Concentrated Aqueous Suspension. *Anal Bioanal Chem.* **2017**, *409* (3), 807−819.
(29) Fox, A. M. *Optical Properties of Solids*; Oxford University Press: 2001.
(30) Sivan, Y.; Baraban, J. H.; Dubi, Y. Experimental Practices Required to Isolate Thermal Effects in Plasmonic Photo-Catalysis: Lessons from Recent Experiments. *OSA Continuum* **2020**, *3* (3), 483−497.
(31) Eftekhari, F.; Escobedo, C.; Ferreira, J.; Duan, X.; Girotto, E. M.; Brolo, A. G.; Gordon, R.; Sinton, D. Nanoholes As Nanochannels: Flow-through Plasmonic Sensing. *Anal. Chem.* **2009**, *81* (11), 4308−4311.
(32) Kumar, S.; Wittenberg, N. J.; Oh, S.-H. Nanopore-Induced Spontaneous Concentration for Optofluidic Sensing and Particle Assembly. *Anal. Chem.* **2013**, *85* (2), 971−977.
(33) Kumar, S.; Wolken, G. G.; Wittenberg, N. J.; Arriaga, E. A.; Oh, S.-H. Nanohole Array-Directed Trapping of Mammalian Mitochondria Enabling Single Organelle Analysis. *Anal. Chem.* **2015**, *87* (24), 11973−11977.
(34) Kumar, S.; Cherukulappurath, S.; Johnson, T. W.; Oh, S.-H. Millimeter-Sized Suspended Plasmonic Nanohole Arrays for Surface-Tension-Driven Flow-Through SERS. *Chem. Mater.* **2014**, *26* (22), 6523−6530.
(35) Sershen, S. R.; Westcott, S. L.; Halas, N. J.; West, J. L. Temperature-Sensitive Polymer-Nanoshell Composites for Photothermally Modulated Drug Delivery. *J. Biomed. Mater. Res.* **2000**, *51* (3), 293−298.
(36) Qiu, G.; Gai, Z.; Tao, Y.; Schmitt, J.; Kullak-Ublick, G. A.; Wang, J. Dual-Functional Plasmonic Photothermal Biosensors for Highly Accurate Severe Acute Respiratory Syndrome Coronavirus 2 Detection. *ACS Nano* **2020**, *14* (5), 5268−5277.
(37) Kurganov, V. A. *HEAT TRANSFER COEFFICIENT*; Begel House: 2011. DOI: 10.1615/AtoZ.h.heat_transfer_coefficient.
(38) Thielicke, W.; Sonntag, R. Particle Image Velocimetry for MATLAB: Accuracy and Enhanced Algorithms in PIVlab. *Journal of Open Research Software* **2021**, *9* (1), 12.

https://doi.org/10.1021/acsnano.2c09938
ACS Nano 2023, 17, 1403−1413